Simulation of bubble migration in a turbulent boundary layer

M. Mattson and K. Mahesh[a)]
Aerospace Engineering and Mechanics, University of Minnesota, 107 Akerman Hall, 110 Union St., Minneapolis, Minnesota 55455-0153, USA

(Received 2 November 2010; accepted 26 January 2011; published online 22 April 2011)

This paper presents the results from a one-way coupled, Euler–Lagrangian, direct numerical simulation of bubbles injected into a turbulent boundary layer. The Reynolds number of the turbulent boundary layer varies from $420 < \mathrm{Re}_\theta < 1800$, and the bubble Reynolds number $\mathrm{Re}_b \sim 1$. Simulation parameters were chosen to match the experiment of Sanders *et al.* [J. Fluid Mech. **552**, 353 (2006)] investigating bubble-induced skin-friction drag reduction in a turbulent boundary layer, although the Reynolds number of the simulation is lower than the experiment. After injection, bubbles move away from the wall as they travel downstream with the flow. Mean bubble diffusion is compared to Sanders *et al.* and the passive scalar diffusion results given by Poreh and Cermak [Int. J. Heat Mass Transfer **7**, 1083 (1964)]. The mean diffusion profiles in the Sanders experiment and the simulation are comparable to the passive scalar results. Except very near the wall, the profiles of bubble concentration are also found to be similar to passive scalar results. The forces on a bubble were analyzed through budgets and the carrier-fluid acceleration was found to be the reason for moving the bubbles away from the wall. © *2011 American Institute of Physics*.
[doi:10.1063/1.3560382]

I. INTRODUCTION

The presence of bubbles in a turbulent boundary layer is known to reduce skin-friction drag. Since the early study by McCormick and Bhattacharyya,[1] much work has been performed to understand the persistence and mechanisms of bubble-induced skin-friction drag reduction (BDR). A canonical configuration to study BDR for marine applications involves the injection of air bubbles into a horizontal turbulent channel or flat-plate boundary layer. As the bubbles travel downstream, the bubbles in the near-wall region modify the near-wall momentum transport, and therefore drag. A comprehensive review of the earliest work has been compiled by Merkle and Deutsch[2] and a review of recent work on BDR and other forms of skin-friction drag reduction has been published by Ceccio.[3] BDR is measured by the ratio of skin-friction coefficient of the bubbly flow (C_f) to the skin-friction coefficient without bubbles ($C_{f,0}$). The mechanisms of BDR, although still not completely understood, are thought to be due to the modification of the near-wall density, viscosity, and turbulent flow by the bubbles. Experiments by Madavan, Deutsch, and Merkle[4] achieved values of BDR up to ~80% and found that BDR increased with increasing gas flow rates and decreasing free-stream flow rates. BDR was found to persist for as much as 70 boundary-layer thicknesses downstream of injection. Gabillet, Colin, and Fabre[5] found that the injection of bubbles increased the turbulent kinetic energy in the region of bubble injection and the void fraction profiles were nearly self-similar. Recent work by Jacob *et al.*[6] obtained BDR using small bubbles and found that even for low bulk bubble concentrations ($C_{bulk} = 0.001$), modification of the turbulent flow by the bubbles was significant downstream of injection in the near-wall region. Sanders *et al.*[7] performed experiments investigating BDR in a high Reynolds number, spatially evolving turbulent boundary layer on a large flat plate ($L = 12.9$ m) in a plate-on-top configuration and found that BDR, although effective near the bubble injection location, lost its effectiveness far downstream from injection.

At large distances downstream from injection, the bubbles migrate away from the wall and drag reduction is lost,[7] making BDR inefficient for large-scale vessels. A reduction of the effectiveness of BDR downstream of injections was also seen by Madavan *et al.*,[4] although BDR was not completely lost due to the length of the test section. Examination of the bubble void fraction downstream of injection by Pal, Merkle, and Deutsch[8] found that the bubble void fraction became more disperse with increasing distance, indicating that the bubbles tended to move away from the wall as they traveled downstream. This bubble migration away from the wall has been found to be the cause for loss of BDR.[7] Much of the work using direct numerical simulation (DNS) to simulate this flow has focused on the mechanisms of BDR.[9–12] However, the mechanisms of bubble dispersion away from the wall are not sufficiently understood.

Gabillet *et al.*[5] derived a model for bubble dispersion using a turbulent boundary-layer profile, although the equations were laminar and assumed a fluid acceleration of zero. Sanders[13] also used a similar approach but included a laminar equation for the fluid acceleration in a turbulent boundary layer. Although these models gave the correct qualitative behavior of bubble diffusion away from the wall, accounting for the turbulent fluctuations on the bubble dispersion is important and, to our knowledge, this subject has not been directly addressed.

We have developed a one-way coupled, Euler–

[a)]Electronic mail: mahesh@aem.umn.edu.

Lagrangian approach and this paper presents the results from simulations of bubbles injected into a spatially evolving turbulent boundary layer, with a focus on the mechanisms of bubble dispersion away from the wall. Simulation parameters were chosen to match the experiment of Sanders *et al.*[7] although the Reynolds number of the simulation is lower than the experiment. This paper is organized as follows. First, a description of the one-way coupled Euler–Lagrangian numerical approach is given (Sec. II). The experiment of Sanders *et al.*,[7] along with the turbulent boundary-layer simulation, is described (Sec. II A). Results for bubble trajectories (Sec. III B), forces on the bubbles, and force budgets are shown (Sec. III C), followed by a discussion of the role of turbulence (Sec. III D) and also bubble size (Sec. III E) on bubble migration away from the wall. A comparison of the behavior of bubble concentration to that of a passive scalar is included in Sec. III F.

II. NUMERICAL APPROACH

In the one-way coupled Euler–Lagrangian framework, the bubbles are modeled as a dispersed phase, with individual bubbles treated as point-particles governed by an equation for bubble motion, combined with a continuous carrier phase described by the Navier–Stokes equations. To solve the Navier–Stokes equations for the continuous phase, a finite-volume approach for unstructured grids[14] is used. This algorithm assumes constant density of the carrier phase and solves the incompressible Navier–Stokes equations using a predictor-corrector approach. This algorithm is discretely energy conserving to ensure robustness at high Reynolds numbers. This method is able to simulate large numbers of bubbles in complex flows. Each bubble is tracked individually and is characterized by its instantaneous position ($\vec{Y}$), velocity ($\vec{v}$), and size (bubble radius R).

Forces from the carrier fluid act upon the bubble and are applied to the bubble's center of mass. The bubble is assumed to be much smaller than the length scales of motion in the carrier phase and the bubbles are modeled as spherical nuclei. Due to a bubble's small size and assuming a dilute concentration of bubbles, the bubbles exert a negligible force on the carrier fluid or other bubbles. This is the one-way coupling regime. The bubble acceleration is equal to the sum of the forces on the bubble. These forces are the drag, lift, fluid acceleration, buoyancy, and added-mass forces,[15–17] yielding

$$m_b \frac{d\vec{v}}{dt} = \sum \vec{F} = \vec{F}_D + \vec{F}_L + \vec{F}_F + \vec{F}_B + \vec{F}_{AM}, \tag{1}$$

with m_b defined as the mass of the bubble and $\vec{v}$ as the bubble velocity.

The drag force $\vec{F}_D$ is due to the viscous friction between the bubble and the carrier fluid. In a shearing flow, the distortion of the local fluid vorticity due to a bubble moving through a fluid produces the lift force $\vec{F}_L$ on the bubble. In an accelerating flow, the bubble will also feel the acceleration of the fluid around it and this force on the bubble is given by $\vec{F}_F$. The buoyancy force $\vec{F}_B$ is a body force due to gravity and is proportional to the difference in density between the bubble and the surrounding fluid. The acceleration of a bubble must also accelerate the surrounding fluid around it. This "added-mass" force on the bubble is given by $\vec{F}_{AM}$. These forces on the bubble are obtained by the following equations:

$$\vec{F}_D = \tfrac{1}{2}\rho_f A_b C_D |\vec{u} - \vec{v}|(\vec{u} - \vec{v}),$$

$$\vec{F}_L = m_f C_L (\vec{u} - \vec{v}) \times \vec{\omega},$$

$$\vec{F}_F = m_f \frac{D\vec{u}}{Dt},$$

$$\vec{F}_B = (m_b - m_f)\vec{g},$$

$$\vec{F}_{AM} = m_f C_M \left(\frac{D\vec{u}}{Dt} - \frac{d\vec{v}}{dt} \right),$$

where the carrier-phase velocity $\vec{u}$ is interpolated to the bubble's instantaneous position and A_b is the area of a circle with radius R, the bubble radius. The mass term m_f is the equivalent mass of a sphere with radius R and the density of the carrier-phase fluid (ρ_f).

Johnson and Hsieh[15] performed Lagrangian simulations of cavitating bubbles traveling around a blunt body and included drag force using a drag coefficient determined by Haberman and Morton[18] and also the contribution of volume change of the bubble over time to the added-mass force. In this paper, the bubbles are assumed to be solid, massless spheres and the volume-variation term is ignored. Thomas *et al.*[16] included contributions due to lift, with a constant lift coefficient of 1/2. Auton, Hunt, and Prud'homme[17] showed that the constant lift coefficient of 1/2 is appropriate in the inviscid limit and that in the added mass and fluid acceleration forces the material derivative of the fluid velocity is the appropriate term for the fluid acceleration.

A constant lift coefficient C_L of 1/2 and a constant added-mass coefficient C_M of 1/2 for a sphere are used.[19,20] Although in the inviscid limit, a lift coefficient of 1/2 is not controversial, at moderate Reynolds numbers the value of the lift coefficient has not been conclusively determined. Sridhar and Katz[21] performed experiments at bubble Reynolds numbers between 20 and 80 and found lift coefficients larger than the inviscid result which also depended on the local vorticity. Legendre and Magnaudet[22] performed numerical simulations of flow over a sphere in weak shear $Sr \leqq 1$, with Sr being the velocity difference across the bubble divided by the relative velocity between the bubble and the carrier fluid, and found lift coefficients that were between 1 and 0.5 for $Re_b > 1$, depending on local vorticity. The lift coefficient approached 1/2 as the Reynolds number increased. The bubble Reynolds number in this work is ~ 1 and the maximum shear parameter $Sr \sim 1$, so using a lift coefficient of 1/2 is not unreasonable. Also, the use of a constant lift coefficient makes factoring out the turbulent contributions to the lift force much less difficult.

The expression for the coefficient of bubble drag, determined experimentally by Haberman and Morton[18] as function of bubble Reynolds number, is given by

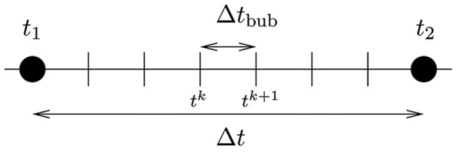

FIG. 1. Discretization of fluid timestep Δt and bubble timestep Δt_{bub} from time t_1 to t_2.

$$C_D = \frac{24}{\text{Re}_b}(1.0 + 0.197\ \text{Re}_b^{0.63} + 2.6 \times 10^{-4}\ \text{Re}_b^{1.38}), \quad (2)$$

where the bubble Reynolds number is defined as $\text{Re}_b = 2R|\vec{u} - \vec{v}|/\nu$. For small bubbles in water, the drag profile is similar to that of solid spheres ($C_D \sim 24/\text{Re}_b$) due to the contamination by surfactants of the bubble surface.

Assuming that the density of gas is much less than that of water, the bubble mass m_b is much less than m_f and the sum of forces on a bubble is zero. After substituting the above expressions for bubble forces into Eq. (1), the following expression is obtained for the time derivative of the bubble velocity:

$$\frac{d\vec{v}}{dt} = \underbrace{-2\vec{g}}_{\text{buoyancy}} + \underbrace{3\frac{D\vec{u}}{Dt}}_{\text{fluid material derivative}} + \underbrace{\frac{3}{4}\frac{C_D}{R}|\vec{u} - \vec{v}|(\vec{u} - \vec{v})}_{\text{drag}} + \underbrace{2C_L(\vec{u} - \vec{v}) \times \vec{\omega}}_{\text{lift}}. \quad (3)$$

The bubble position and velocity over time are determined by integrating the bubble acceleration equation [Eq. (3)]. The simulation is broken into two different timescales: the Eulerian fluid timestep Δt and the path integration timestep of the bubbles Δt_{bub}, where $\Delta t = t_2 - t_1$ and $\Delta t_{\text{bub}} = t^{k+1} - t^k$ (see Fig. 1). The Eulerian fluid variables are known at $t = t_1$ and $t = t_2$ from the advancement of the Navier–Stokes equations, which in a one-way coupled approach are integrated independently of the bubble time advancement.

The Eulerian values in Eq. (3) must be evaluated at time $t = t^k$ and at the bubble position $\vec{x} = \vec{Y}^k$ on unstructured grids. Spatial gradients of the carrier-phase parameters at the control volume centroids are obtained using a least-squares method. The fluid velocity at the bubble location $\vec{u}|_{x=Y^k}$ is interpolated from the values at the control volume centroid by

$$\vec{u}(t^k)|_{\vec{x}=\vec{Y}^k} = \vec{u}(t^k)|_{\vec{x}_{cv}} + [(\vec{Y}^k - \vec{x}_{cv}) \cdot \vec{\nabla}]\vec{u}(t^k)|_{\vec{x}_{cv}}. \quad (4)$$

The spatial gradients $\partial u_i/\partial x_j$ are determined at the control volume centroids by a least-squares approach. To obtain the control volume values required in Eq. (4) at time $t = t^k$, a linear time interpolation of the fluid velocity is performed using

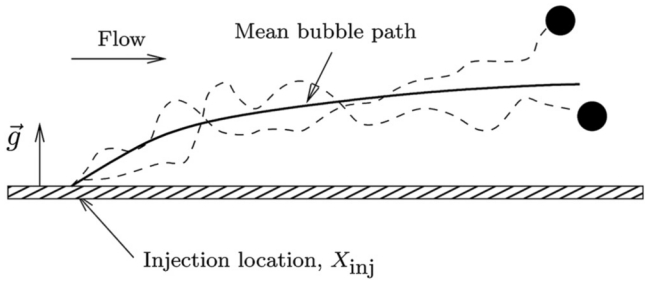

FIG. 2. Schematic of boundary layer and bubble paths. Dashed lines denote the paths taken by individual bubbles and the solid line represents the ensemble-averaged path of all bubbles.

$$u_i(t^k) = \frac{1}{\Delta t}[(t^k - t_1)u_i(t_2) + (t_2 - t^k)u_i(t_1)]. \quad (5)$$

The velocity at time $t = t^{k+1}$ is integrated using the Adams–Bashforth approach,

$$v_i^{k+1} = v_i^k + \Delta t_{\text{bub}}\left(\frac{3}{2}\frac{dv_i}{dt}^k - \frac{1}{2}\frac{dv_i}{dt}^{k-1}\right). \quad (6)$$

Once the bubble velocity has been integrated to $t = t^{k+1}$, the bubble position is integrated using the trapezoidal method,

$$Y_i^{k+1} = Y_i^k + \frac{\Delta t_{\text{bub}}}{2}(v_i^{k+1} + v_i^k). \quad (7)$$

The bubble equations are advanced from $k, k+1, k+2$, etc. until $t = t_2$ is reached. Then the fluid equations are advanced and the bubble integration process begins anew.

Bubble-wall interactions are treated as hard-sphere, inelastic collisions and bubble-bubble interactions are ignored. This approach can simulate flows with large numbers of bubbles in complex geometries over a wide range of Reynolds numbers.

A. Computational and physical parameters

Sanders *et al.*[7] performed experiments investigating BDR in a high Reynolds number, spatially evolving turbulent boundary layer on a large flat plate ($L = 12.9$ m). These experiments were performed in the plate-on-top configuration, where the buoyancy force is acting to push the bubbles toward the wall. Figure 2 shows the typical bubble behavior in this experiment. Bubble size distributions and bubble-to-fluid area ratio were also measured at two downstream locations ($x = X_1, X_2$). Increasing the air flow-rate of injection Q_a and/or reducing free-stream velocity U_e increased BDR. For cases with the lowest free-stream velocity, the bubbles coalesced into a continuous layer of gas and drag reduction was maintained far downstream. For all other free-stream speeds and air-injection rates, the skin-friction drag was reduced downstream ($C_f/C_{f,0} < 1$) of the bubble injection location, but increased with downstream distance and approached single-phase levels ($C_f/C_{f,0} \to 1$). In these experiments, the near-wall bubble concentration became more dilute with downstream distance and eventually a bubble-free liquid layer formed near the wall.

TABLE I. Simulation parameters.

Case	$L_x/L_{\text{ref}} \times L_y/L_{\text{ref}} \times L_z/L_{\text{ref}}$	$N_x \times N_y \times N_z$
Bubbly flow	$40 \times 3.12 \times 1.57$	$1600 \times 132 \times 256$
Inflow generation	$10 \times 3.12 \times 1.57$	$100 \times 45 \times 64$

For the low air-injection rate ($Q_a = 0.05\ \text{m}^3\ \text{s}^{-1}$) and high flow speed ($U_e > 18\ \text{ms}^{-1}$) in the experiments of Sanders *et al.*,[7] the skin-friction reduction as compared to the single-phase case was very small ($C_f/C_{f,0} > 0.95$) for small distances downstream ($x < 2$ m) and approached single-phase results further downstream. This experiment will now be defined as case S1.

Due to the large Reynolds numbers in this turbulent boundary layer ($\text{Re}_\theta > 15\,000$), providing sufficient resolution of the turbulent flow with DNS is prohibitively expensive. The Reynolds number of the boundary layer is reduced ($420 < \text{Re}_\theta < 1800$) in simulations while matching the ratio of mean bubble injection radius to boundary-layer size at injection. For experiment S1, the mean bubble radius and boundary-layer thickness were measured at downstream station X_1. The mean bubble diameter at $x = X_1$ was 230 μm. Assuming a constant bubble radius and using a power law to estimate boundary-layer thickness, the ratio of bubble size to boundary-layer thickness at injection is obtained ($R_{\text{inj}}/\delta_{99,\text{inj}} \approx 0.0064$) and matched in the simulation. The Froude number based on the boundary-layer thickness at injection ($\text{Fr} = U_e/\sqrt{g_y \delta_{99,\text{inj}}}$) is 46. The distance between X_1 and X_{inj}, nondimensionalized by the boundary-layer thickness (δ_{99}) at injection, is 35.6. The outflow of the bubble simulation is located at $(x - X_{\text{inj}})/\delta_{99,\text{inj}} = 67$. The bubble injection velocity is zero in the streamwise and spanwise directions and the wall-normal injection velocity v_y/U_e is 0.55, as given in the Sanders[13] model of bubble diffusion in a turbulent boundary layer.

A separate simulation is required to provide the necessary inflow turbulence for the spatially evolving turbulent boundary-layer simulation. The inflow-generation simulation applies rescaling to the streamwise boundary conditions[23] to obtain turbulent boundary-layer flow in a reasonably sized domain. A velocity plane from the inflow simulation is then interpolated to the inflow plane of the bubbly flow simulation. The domain lengths (L) and the number of control volumes (N) in the x (streamwise), y (wall-normal), and z (spanwise) directions are given in Table I. The bulk Reynolds number $\text{Re} = U_e L_{\text{ref}}/\nu$ is equal to 14 000 with $L_{\text{ref}} = \delta_{99,\text{inj}}/0.52$. At the inflow of the inflow-generation simulation, the Reynolds number based on the momentum thickness (Re_θ) is 420, while at the inflow of the bubbly flow domain, the Reynolds number $\text{Re}_\theta = 600$ and $\text{Re}_\theta = 1800$ at the outflow. The grid spacing is uniform in the streamwise and spanwise directions and nonuniform in the wall-normal direction. For the bubbly flow domain, $\Delta y_{\text{min}}/L_{\text{ref}} = 5.07 \times 10^{-4}$, with $\Delta y^+_{\text{min}} = 0.31$ and 13 control volumes are within $\Delta y^+ < 10$ at $(x - X_{\text{inj}})/\delta_{99,\text{inj}} = 45.4$. For the inflow-generation domain, $\Delta y_{\text{min}}/L_{\text{ref}} = 1.96 \times 10^{-3}$, with $\Delta y^+_{\text{min}} = 1.38$ and six control volumes are within $\Delta y^+ < 10$ at $(x - X_{\text{inj}})/\delta_{99,\text{inj}} = -9.6$.

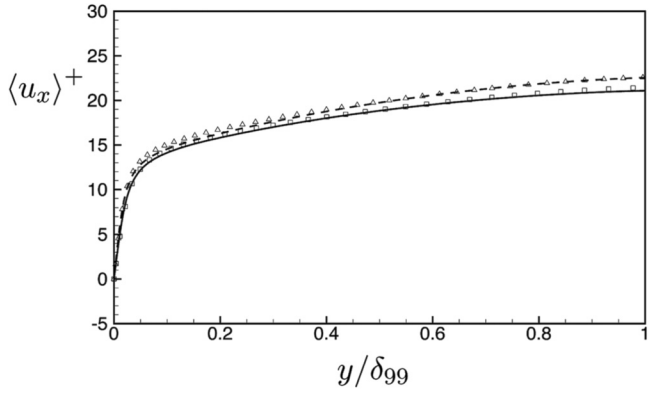

FIG. 3. Comparison of mean streamwise velocity to results from the Simens *et al.* (Ref. 24) simulation. —, DNS, ($\text{Re}_\theta = 1100$); - -, DNS, ($\text{Re}_\theta = 1551$); □, Simens, ($\text{Re}_\theta = 1100$); △, Simens, ($\text{Re}_\theta = 1551$).

The inflow-generation simulation was initialized from a previous boundary layer simulation and run for $t^* = tU_e/L_{\text{ref}} = 420$ units of time to ensure removal of all transients, with a constant timestep of $\Delta t^* = 0.08$. Statistics were taken from $420 < t^* < 4400$, and the velocity inflow plane and additional statistics were sampled from $4400 < t^* < 8900$. The bubbly flow simulation was initialized from zero velocity and run for 1500 units of time to remove all transients with $\Delta t^* = 0.015$. One hundred bubbles were then injected every ten fluid timesteps at a random spanwise location near the wall ($y_{\text{inj}}/\delta_{99,\text{inj}} = 2 \times 10^{-6}$). The bubble timestep Δt^*_{bub} was equal to 1.5×10^{-5}. Fluid statistics and bubble statistics were sampled from $1500 < t^* < 2100$ until convergence was achieved.

III. RESULTS

A. Carrier-phase turbulence

Results for the carrier-phase turbulent flow in the bubbly flow simulation are given in Figs. 3 and 4. The results shown are taken from two streamwise locations, one at $\text{Re}_\theta = 1100$ and another at $\text{Re}_\theta = 1551$. The wall-normal distance is nondimensionalized by the boundary-layer thickness δ_{99} at each streamwise location. The carrier flow shows a good agreement with results from Simens *et al.*[24] for both the mean flow and turbulence intensities.

B. Bubble trajectories

After injection, the bubbles tend to disperse and travel away from the wall, as shown in the instantaneous snapshots of bubble position in Fig. 5. Note that near the injection, the bubbles are concentrated into filament-like structures that break down with increasing downstream distance. Through the force due to the fluid acceleration, bubbles are pushed toward the centers of vortex cores. This preferential concentration of bubbles in vortex cores has been observed in previous simulations of bubbles in homogeneous, isotropic turbulence.[25] Near the wall in a turbulent boundary-layer

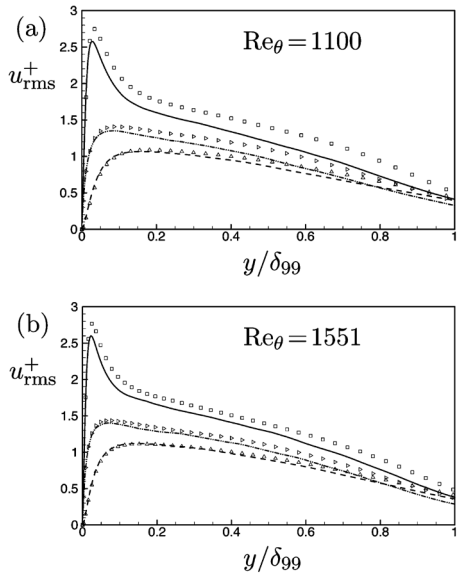

FIG. 4. Comparison of turbulence intensities to results from the Simens *et al.* (Ref. 24) simulation. (a) rms of the turbulence intensities vs wall-normal distance for Re_θ=1100. (b) rms of the turbulence intensities vs wall-normal distance for Re_θ=1551. —, $u^+_{x,\mathrm{rms}}$, DNS; - -, $u^+_{y,\mathrm{rms}}$, DNS; -···-, $u^+_{z,\mathrm{rms}}$, DNS; □, $u^+_{x,\mathrm{rms}}$, Simens; △, $u^+_{y,\mathrm{rms}}$, Simens; ▷, $u^+_{z,\mathrm{rms}}$, Simens.

flow, vortical structures that form the legs of hairpin structures are oriented in the streamwise direction.[26] The tendency of bubbles to form filament-like structures observed in Fig. 5(c) is due to the attraction of the bubbles to the streamwise vortical structures. The bubbles tend to travel away from the wall as they move downstream, as observed in Sanders *et al.*[7]

An ensemble-average is obtained by a number average performed over all bubbles. The ensemble-average is a function of the residence time of a bubble in the flow after injection ($t_r = t - t_{\mathrm{inj}}$). In this paper, ensemble-averaged bubble quantities are denoted by the subscript "e." The ensemble-average of f at time t_r is given by

$$\langle f(t_r)\rangle_e = \frac{1}{N}\sum_{i=1}^{N} f(t_r), \tag{8}$$

where $\langle f(t_r)\rangle_e$ is sampled over N number of bubbles. Sampling of quantities for the ensemble-average was performed at discrete lengths of residence time after injection (i.e., $t_r = n\Delta t_r$ for $n = 1,2,3,\ldots$), where $\Delta t_r = 120\Delta t$. This time interval Δt_r was chosen to obtain samples at a quick enough rate to resolve bubble behavior but not so often as to become unnecessarily expensive to compute.

Figure 6 shows the ensemble-averaged bubble trajectory, with the tendency of the bubbles to travel away from the wall clearly evident. Figure 7 plots the ensemble-averaged bubble velocities as a function of ensemble-averaged streamwise position. The wall-normal velocity is positive (away from the wall) and approaches a constant value with increasing downstream distance. As the bubbles travel downstream, the streamwise velocity increases due to the bubbles accelerating along with the fluid as they enter the higher-momentum flow away from the wall. The ensemble-averaged fluctuations of bubble position and velocity are plotted in Figs. 8 and 9. Streamwise fluctuations are large as compared to wall-normal position fluctuations due to the large velocity fluctuations along the streamwise direction. The fluctuations in position increase with downstream distance due to dispersion. The bubble velocity fluctuations increase to a maximum value just downstream of injection then decrease and approach a constant value as the bubble travels downstream.

C. Budgets of bubble acceleration

The mean acceleration $\langle d\vec{v}/dt\rangle_e$ can be integrated to obtain the mean velocity $\langle \vec{v}\rangle_e$ and integrated once again to give the mean position $\langle \vec{Y}\rangle_e$, so understanding the forces on the bubble provides insight that can be used to predict bubble dispersion. The drag, lift, fluid acceleration, and buoyancy

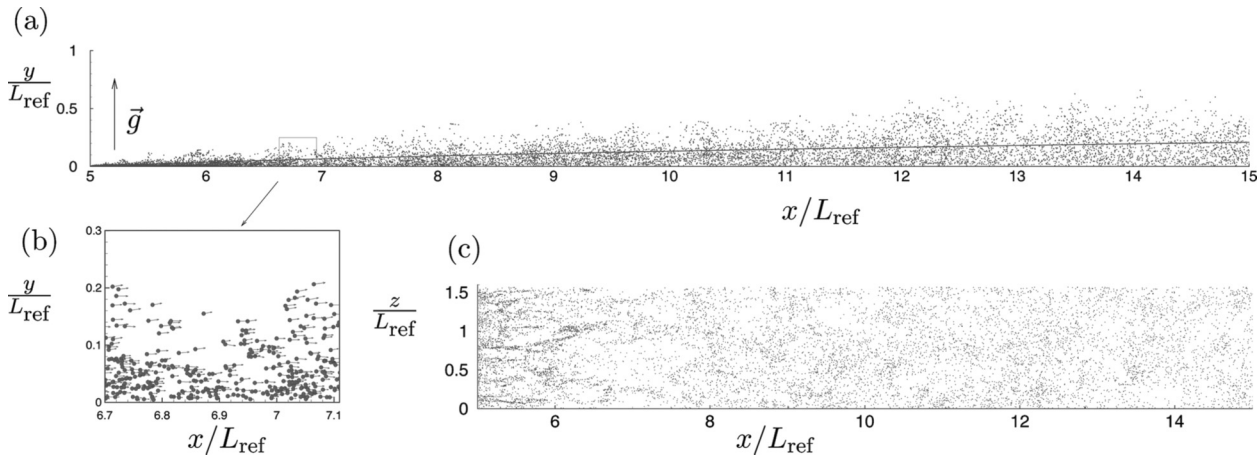

FIG. 5. Instantaneous bubble position with only a part of the domain shown ($5 < x < 15$). (a) Bubble position in streamwise and wall-normal coordinates with ensemble-averaged position $\langle Y_y\rangle_e$ vs $\langle Y_x\rangle_e$ shown by the black line. (b) Close-up view of (a) along with bubble velocity vectors (v_x, v_y). (c) Bubble position in streamwise and spanwise coordinates.

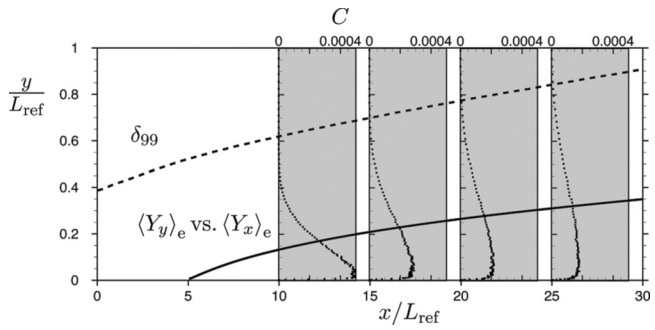

FIG. 6. Ensemble-averaged bubble trajectory and evolution of boundary-layer thickness along with bubble concentration profiles. Bubble concentration C is plotted vs y/L_{ref} at x/L_{ref}=10, 15, 20, and 25. - -, δ_{99}; —, $\langle Y_y\rangle_e$ vs $\langle Y_x\rangle_e$; ■, C.

terms in Eq. (3) can be ensemble-averaged to obtain a budget of mean bubble acceleration. The equation for ensemble-averaged bubble acceleration is

$$\left\langle \frac{d\vec{v}}{dt} \right\rangle_e = \langle -2\vec{g}\rangle_e + \left\langle 3\frac{D\vec{u}}{Dt} \right\rangle_e + \left\langle \frac{3}{4}\frac{C_D}{R}|\vec{u}-\vec{v}|(\vec{u}-\vec{v}) \right\rangle_e + \langle 2C_L(\vec{u}-\vec{v})\times\vec{\omega}\rangle_e. \quad (9)$$

Budgets of mean bubble acceleration as a function of distance downstream of injection for bubbles in the turbulent boundary layer are shown in Figs. 10 and 11. Note that for the streamwise accelerations, the drag and lift contributions accelerate the bubble in the downstream direction while the fluid acceleration tends to slow the bubbles, except for a short period near injection where the fluid acceleration is positive. The drag acceleration is positive, therefore the difference in velocity in the streamwise direction $\langle u_x\rangle_e - \langle v_x\rangle_e$ is greater than zero. The ensemble-averaged bubble acceleration is always positive and approaches zero for large distances downstream of injection.

Figure 11 plots the budgets of the ensemble-averaged accelerations in the wall-normal direction. From Fig. 11(a), it is clear the drag and fluid accelerations have the largest magnitudes. In the drag acceleration, the difference in velocity in the wall-normal direction $\langle u_y\rangle_e - \langle v_y\rangle_e$ is less than zero, therefore the bubbles (in an ensemble-averaged sense) have a larger wall-normal velocity than the Eulerian fluid. Figure 11(b) plots the bubble acceleration in the wall-normal direction, with the drag and fluid acceleration terms summed together. The total sum of fluid and drag accelerations pushes the bubbles away from the wall. In Fig. 11(b), the bubble acceleration depends on distance from the injection location. Far downstream of injection, the lift acceleration and the sum of the fluid and drag acceleration are constant. The total bubble acceleration approaches zero. Near injection, the bubble acceleration terms vary with distance from injection location. The total acceleration is positive near injection and decreases with downstream distance, approaching zero for large downstream distances.

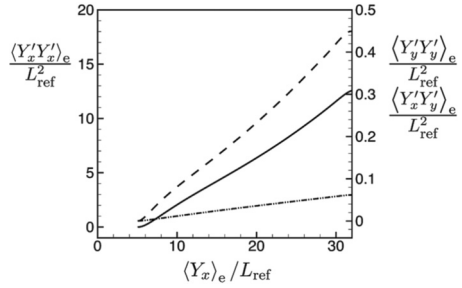

FIG. 8. Ensemble-averaged position fluctuations. —, $\langle Y'_xY'_x\rangle_e$; - -, $\langle Y'_yY'_y\rangle_e$; -···-, $\langle Y'_xY'_y\rangle_e$.

The ensemble-averaged terms of Eq. (9) can be broken down into constituents of ensemble-averaged mean and fluctuating terms. For incompressible flow, the divergence of the fluid velocity is zero. It can be easily shown that when the carrier-phase velocity is broken into its mean and fluctuating terms, $u_i=\langle u_i\rangle_e+u'_i$, the divergence of the mean and fluctuating terms are also zero.

Starting with the equation for the drag acceleration,

$$\langle \vec{A}_D\rangle_e = \left\langle \frac{3}{4}\frac{C_D}{R}|\vec{u}-\vec{v}|(\vec{u}-\vec{v}) \right\rangle_e, \quad (10)$$

the drag expression can be approximated by using only the first-order term for the drag coefficient, $C_D \sim 24/\mathrm{Re}_b$, since $\mathrm{Re}_b \sim 1$. This results in a simplification of the drag acceleration to

$$A_{D,i} = \frac{9\nu}{R^2}(u_i - v_i). \quad (11)$$

If the bubble radius is constant, taking the ensemble-average of the above expression results in

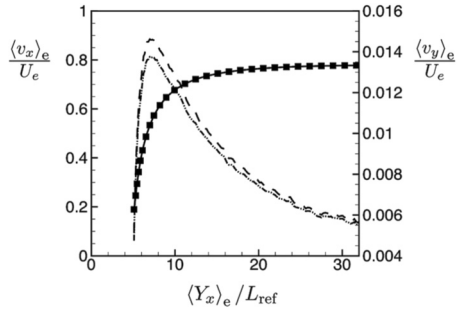

FIG. 7. Ensemble-averaged bubble and carrier-fluid velocities. —, $\langle v_x\rangle_e$; - - -, $\langle v_y\rangle_e$; ■, $\langle u_x\rangle_e$; -···-, $\langle u_y\rangle_e$.

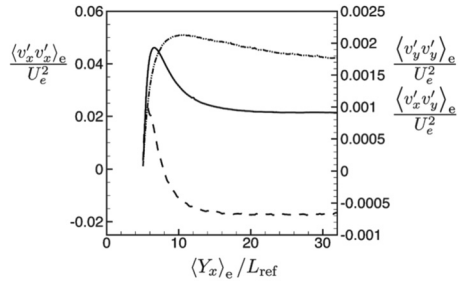

FIG. 9. Ensemble-averaged velocity fluctuations. —, $\langle v'_xv'_x\rangle_e$; - -, $\langle v'_yv'_y\rangle_e$; -···-, $\langle v'_xv'_y\rangle_e$.

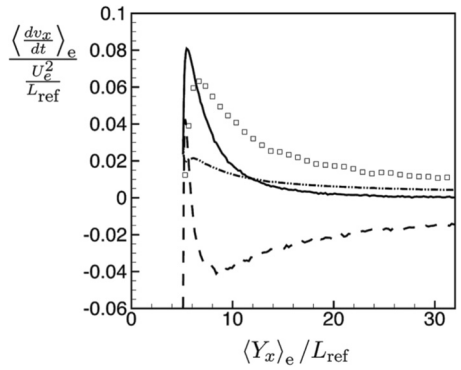

FIG. 10. Ensemble-averaged bubble acceleration budget in the streamwise (x) direction. - -, $3(Du_x/Dt)$; □, Drag_x; -···-, Lift_x; —, Total_x.

$$\langle \vec{A}_D \rangle_{e,approx} = \frac{9\nu}{R^2}(\langle u_i \rangle_e - \langle v_i \rangle_e), \tag{12}$$

where only the mean quantities of velocity remain. Figure 12 plots the comparison of the results of Eq. (12) to the measured ensemble-averaged acceleration in the y-direction. Good agreement between the approximate equation and measured quantities is obtained.

The ensemble-averaged fluid acceleration can be expanded to obtain

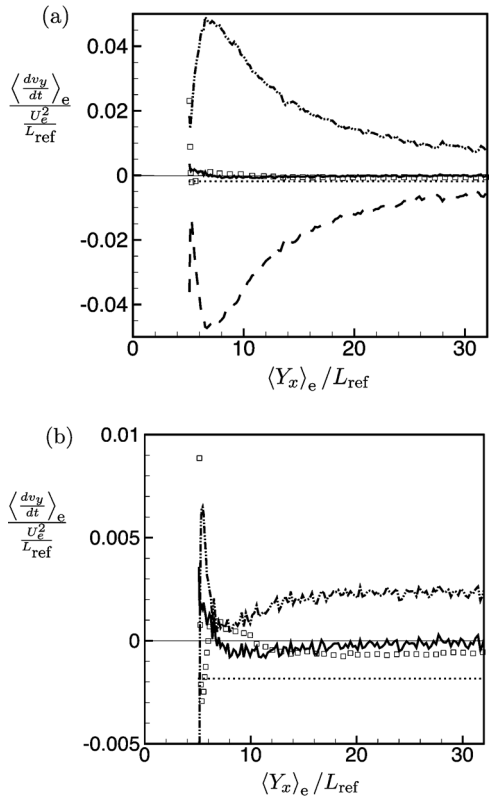

FIG. 11. Ensemble-averaged bubble acceleration budget in the wall-normal (y) direction. (a) Normal view showing all terms individually. - -, Drag_y; -···-, $3(Du_y/Dt)$; □, Lift_y; ···, $-2g$; —, Total_y. (b) Zoomed-in view with the drag and fluid acceleration terms summed together. -···-, [Drag_y $+3(Du_y/Dt)$]; □, Lift_y; ···, $-2g$; —, Total_y.

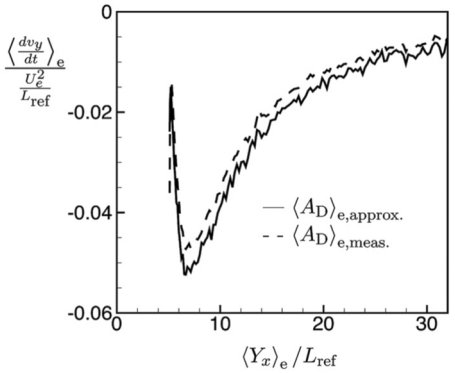

FIG. 12. Comparison of drag acceleration in the wall-normal direction for the approximate equation and measured result.

$$\langle A_{F,i} \rangle_e = 3\frac{\partial \langle u_i \rangle_e}{\partial t} + 3\langle u_j \rangle_e \frac{\partial \langle u_i \rangle_e}{\partial x_j} + 3\frac{\partial}{\partial x_j}\langle u_i' u_j' \rangle_e. \tag{13}$$

The contributions of the unsteady, mean, and fluctuating terms in the fluid acceleration term are shown in Fig. 13. The largest terms are the unsteady term $\partial \langle u_y \rangle_e / \partial t$, which is positive, and the mean gradient term $\langle u_j \rangle_e \partial \langle u_y \rangle_e / \partial x_j$, although the fluctuating term also has a significant contribution. For the mean gradient, the $\langle u_x \rangle_e \partial \langle u_y \rangle_e / \partial x$ contribution is the largest and negative since $\partial \langle u_y \rangle_e / \partial x$ is negative due to boundary-layer growth.

The lift acceleration is

$$\langle \vec{A}_L \rangle_e = \langle 2C_L(\vec{u} - \vec{v}) \times \vec{\omega} \rangle_e,$$

and can also be factored into mean and fluctuating terms. By applying the vector triple product, the ensemble-averaged lift equation becomes

$$\begin{aligned} \langle A_{L,i} \rangle_e = {} & \langle u_j \rangle_e \frac{\partial \langle u_j \rangle_e}{\partial x_i} + \left\langle u_j' \frac{\partial u_j'}{\partial x_i} \right\rangle_e - \langle u_j \rangle_e \frac{\partial \langle u_i \rangle_e}{\partial x_j} \\ & - \left\langle u_j' \frac{\partial u_i'}{\partial x_j} \right\rangle_e - \langle v_j \rangle_e \frac{\partial \langle u_j \rangle_e}{\partial x_i} - \left\langle v_j' \frac{\partial u_j'}{\partial x_i} \right\rangle_e \\ & + \langle v_j \rangle_e \frac{\partial \langle u_i \rangle_e}{\partial x_j} + \left\langle v_j' \frac{\partial u_i'}{\partial x_j} \right\rangle_e. \end{aligned} \tag{14}$$

Taking the above equation, the last four terms are similar

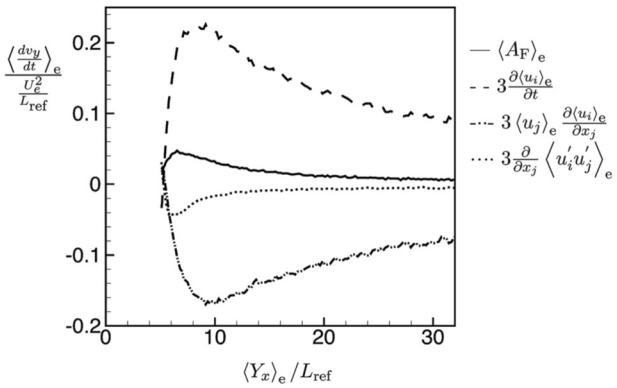

FIG. 13. Budget of fluid acceleration in the y-direction.

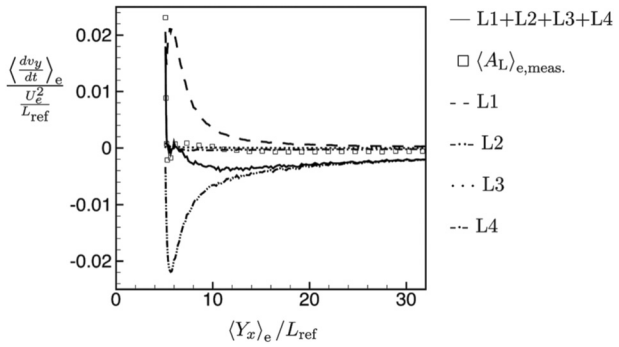

FIG. 14. Budget of lift acceleration in the y-direction.

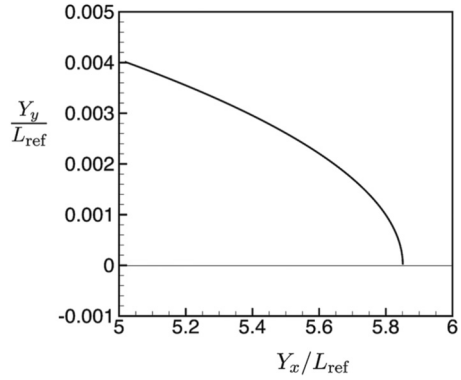

FIG. 15. Bubble trajectory in the laminar boundary layer.

with respect to the first four, except for having a sign change and a substitution of the bubble velocity for the fluid velocity. These terms can be grouped together to see more easily the total contribution to the lift acceleration. The equation of the summed terms is now grouped into four terms,

$$\langle A_{\mathrm{L},i}\rangle_{\mathrm{e}} = \underbrace{(\langle u_j\rangle_{\mathrm{e}} - \langle v_j\rangle_{\mathrm{e}})\frac{\partial\langle u_j\rangle_{\mathrm{e}}}{\partial x_i}}_{\mathrm{L1}} + \underbrace{\left\langle u_j'\frac{\partial u_j'}{\partial x_i}\right\rangle_{\mathrm{e}} - \left\langle v_j'\frac{\partial u_j'}{\partial x_i}\right\rangle_{\mathrm{e}}}_{\mathrm{L2}}$$

$$+ \underbrace{(\langle v_j\rangle_{\mathrm{e}} - \langle u_j\rangle_{\mathrm{e}})\frac{\partial\langle u_i\rangle_{\mathrm{e}}}{\partial x_j}}_{\mathrm{L3}} \underbrace{- \left\langle u_j'\frac{\partial u_i'}{\partial x_j}\right\rangle_{\mathrm{e}} + \left\langle v_j'\frac{\partial u_i'}{\partial x_j}\right\rangle_{\mathrm{e}}}_{\mathrm{L4}}. \quad (15)$$

Figure 14 plots the summed contributions of each similar term to the total lift acceleration. The two largest terms are L1 and L2, with L3 and L4 being negligible. The sum of L1–L4 is given by the solid black line, and an independently measured ensemble-average of the lift acceleration is given by open symbols. Even though there is some discrepancy in the lift acceleration budget to the total ensemble-averaged value of lift, it is clear that the terms L1 and L2 are the dominant contributors and Eq. (14) can be reduced to

$$\langle A_{\mathrm{L},i}\rangle_{\mathrm{e,approx}} = \langle u_j\rangle_{\mathrm{e}}\frac{\partial\langle u_j\rangle_{\mathrm{e}}}{\partial x_i} + \left\langle u_j'\frac{\partial u_j'}{\partial x_i}\right\rangle_{\mathrm{e}} - \langle v_j\rangle_{\mathrm{e}}\frac{\partial\langle u_j\rangle_{\mathrm{e}}}{\partial x_i} - \left\langle v_j'\frac{\partial u_j'}{\partial x_i}\right\rangle_{\mathrm{e}}. \quad (16)$$

Through factoring out the mean and fluctuating terms in the ensemble-averaged accelerations and comparing budgets, the full equations can be reduced from their full form. For small $\mathrm{Re_b}$, using only mean contributions to calculate the mean drag acceleration is appropriate. In the fluid acceleration term, the unsteady and mean convection terms are largest, although the fluctuating term is not negligible. The equation for lift can be simplified from the original eight terms to four. If the mean and fluctuating terms in the bubble acceleration equations can be modeled, the mean diffusion of the bubbles away from the wall can be determined over a range of Reynolds numbers.

D. Role of turbulence: Bubbles in a laminar boundary layer

Turbulence significantly affects bubble dispersion in a turbulent boundary layer. Without turbulence there is a lack of intermittency of the forces on the bubbles and no migration of bubbles away from the wall. To demonstrate this, a simulation with bubbles injected into a laminar boundary layer was performed. The outer scales were matched between the turbulent and laminar simulations at the injection location, with $\mathrm{Re}=14\,000$ and $R/\delta_{99,\mathrm{inj}}=0.0064$. The bubble radius was kept constant throughout the simulation. A simulation domain of $L_x/L_{\mathrm{ref}}=40$, $L_y/L_{\mathrm{ref}}=3.12$, and $L_z/L_{\mathrm{ref}}=1.57$ was used, with $N_x=400$, $N_y=45$, and $N_z=64$. The grid was uniform in the streamwise and spanwise directions, but nonuniform in the wall-normal direction with the smallest wall-normal spacing near the wall. The simulation was initialized with the Blasius solution[27] and then advanced until the velocity field was converged. Good agreement between velocity field and Blasius solution was obtained.

In this laminar flow, the forces on the bubble are greatly simplified as compared to turbulent flow, with no fluctuating terms in the bubble acceleration equations. The bubble is injected with a positive wall-normal velocity and travels slightly into the boundary layer (Fig. 15). The bubble penetrates only a small distance into the boundary layer due to drag and then travels toward the wall, opposite of what is seen in the turbulent case. Because the size of the bubble is on the same scale as the penetration distance, the simulation was allowed to continue to run without any particle-wall boundary conditions (such as bubble-wall collisions) until the bubble center reached the wall.

As seen in Fig. 16, the forces on the bubble are constant throughout the bubble path, except very near injection where a large drag force quickly damps out the initial injection velocity of the bubble. This happens very quickly with respect to the other scales in the flow and is not shown in Fig. 16 or the other figures of laminar flow. The lift force and fluid acceleration in the wall-normal direction are both zero and the drag exactly counterbalances the buoyancy force. The bubble has reached its terminal velocity according to the equation

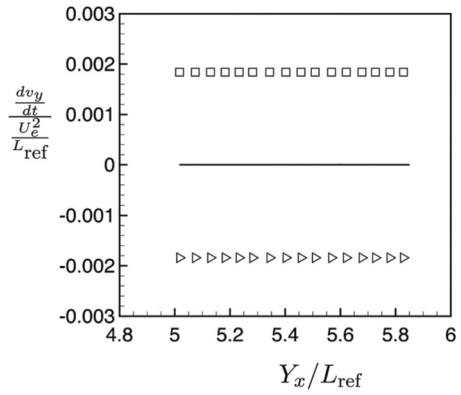

FIG. 16. Bubble acceleration budget in the wall-normal (y) direction for the laminar boundary-layer simulation. □, Drag$_y$; ▷, $-2g$; —, Total$_y$.

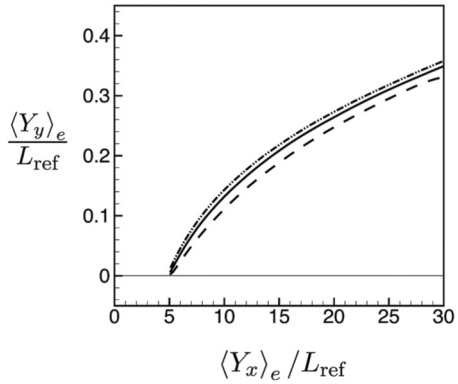

FIG. 17. Bubble trajectories for three differently sized bubbles in a turbulent boundary layer. - -, $R/\delta_{99,inj}=0.0037$; —, $R/\delta_{99,inj}=0.0064$; -···-, $R/\delta_{99,inj}=0.0092$.

$$\frac{dv_y}{dt} = -2g + \frac{3}{4}\frac{C_D}{R}|\vec{u}-\vec{v}|(u_y - v_y), \tag{17}$$

and since the terms on the right hand side balance each other at steady state and $C_D \sim 24/\mathrm{Re_b}$,

$$2g = \frac{9\nu}{R^2}(u_y - v_y), \tag{18}$$

and the bubble has a constant velocity in the wall-normal direction of $v_y/U_e = -3.1\times10^{-5}$, since $u_y \approx 0$ near the wall.

When comparing the turbulent and laminar boundary-layer (LBL) simulations, there are large differences in the overall behavior of the bubbles. The mean trajectory of the LBL shows bubbles traveling toward the wall, while the turbulent boundary layer shows the bubbles dispersing away from the wall as they travel downstream. The influence of the injection velocity is weak in both simulations, as the drag force quickly damps out the initial injection velocity. At this Reynolds number, the injection velocity of the bubbles can be ruled out as a mechanism for bubble dispersion away from the wall.

The dispersion of bubbles away from the wall is directly dependent on the turbulence. In the LBL, the fluid acceleration in the wall-normal direction is zero, and the bubbles travel toward the wall due to buoyancy. In the turbulent boundary layer (TBL), the fluid acceleration is large and pushes the bubbles away from the wall. In comparing the TBL and LBL simulations, it is evident that the turbulent fluid acceleration is the mechanism for bubble diffusion.

E. Effect of bubble size

To determine the effect of bubble size, a simulation with three bubble sizes ($R=R_1,R_2,R_3$) was performed, with R_2 equal to the mean bubble radius in Sanders *et al.*,[7] and R_1 and R_3 equal to $R_2 \pm \sigma_{dev}$, where σ_{dev} is the experimental standard deviation of bubble size measured at $x=X_1$. All other conditions were the same as the previous turbulent bubble simulation. The change in size is on the order of R_2, with $R_1/\delta_{inj}=0.0037$, $R_2/\delta_{inj}=0.0064$, and $R_3/\delta_{inj}=0.0092$.

The trajectories of the bubbles are shown in Fig. 17. The bubbles with the largest size penetrate farther into the turbulent boundary layer than smaller bubbles due to an increased wall-normal velocity after injection. The mechanism for the enhanced movement away from the wall for larger bubbles is found by looking at the acceleration budget in the wall-normal direction. From the approximate drag equation [Eq. (12)], the drag acceleration is inversely proportional to R^2 and the larger bubbles initially have a reduced drag force and are less likely to follow the fluid flow. This leads to an increased relative velocity, which increases the lift and drag accelerations overall [Figs. 18(a) and 18(c)]. The fluid acceleration also increases for larger bubbles due to an increase in the unsteady velocity contribution [Fig. 18(b)]. The larger bubbles are moving upward into higher-momentum flow more quickly than smaller bubbles, therefore $\partial\langle u_y\rangle_e/\partial t$ is increased. Altogether, this leads to an ensemble-average path that is farther away from the wall for larger bubbles than smaller bubbles.

F. Comparison to a passive scalar

Poreh and Cermak[28] investigated the diffusion of a passive scalar by injecting ammonia gas into a turbulent boundary layer of air and then measuring the scalar concentration downstream of injection. As the gas traveled downstream with the flow, the mean concentration of ammonia decreased near the wall. Except very near the wall, this behavior is similar to what is seen for bubbles injected into a turbulent boundary layer, even though the bubbles are not passive scalars.

Poreh and Cermak[28] defined two length scales, δ_{av} and λ, with δ_{av} based on the local boundary-layer thickness and λ being the wall-normal position where the time-averaged concentration was equal to one half of the maximum concentration at that streamwise location, $C(\lambda)=1/2C_{max}$. The passive scalar data were found to behave differently in four zones that are defined as a function of $(x-X_{inj})/\delta_{av}$. The initial zone is near injection, $(x-X_{inj})/\delta_{av} \le 2$. In this region, the physics of injection is likely to affect the diffusion behavior. The intermediate zone is defined as the region between $2 \le (x-X_{inj})/\delta_{av} \le 18$, the transition zone is defined as the region of $18 \le (x-X_{inj})/\delta_{av} \le 60$, and the final zone where $(x-X_{inj})/\delta_{av} > 18$.

Figure 19 shows the behavior of λ/δ_{99} versus

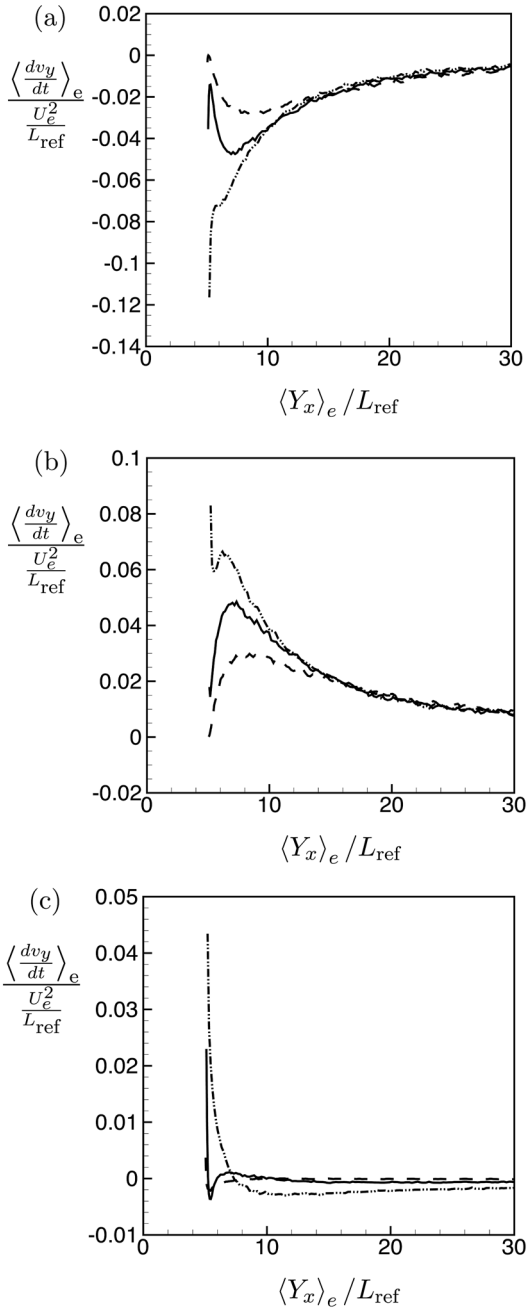

FIG. 18. Bubble acceleration in the wall-normal direction for three differently sized bubbles in a turbulent boundary layer with (a) plotting the drag acceleration, (b) the fluid acceleration, and (c) the lift acceleration. - -, $R/\delta_{99,inj}=0.0037$; —, $R/\delta_{99,inj}=0.0064$; -···-, $R/\delta_{99,inj}=0.0092$.

$(x-X_{inj})/\delta_{av}$ for the results of Poreh and Cermak.[28] Also included in this figure are diffusion profiles of temperature by Wieghardt,[29] bubbles in a turbulent boundary layer by Sanders *et al.*,[7] and the DNS data of bubble diffusion. The diffusion length scale λ increases as the scalar and bubbles move downstream. The near-wall concentration of passive scalar and bubbles decreases with downstream distance. For a passive scalar in the intermediate zone, λ/δ_{99} follows a power law as a function of $(x-X_{inj})/\delta_{av}$. In the transition zone, λ/δ_{99} approaches 0.64, the value of λ/δ_{99} in the final zone.

In the intermediate zone, Poreh and Cermak[28] found that

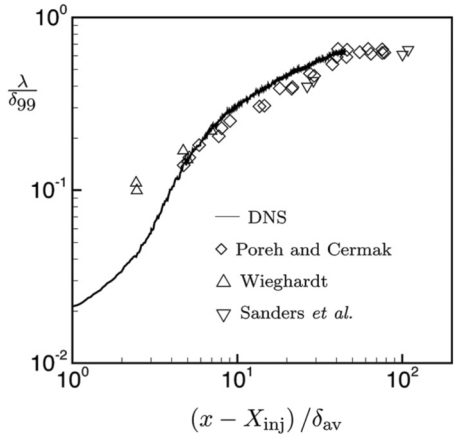

FIG. 19. Diffusion of a passive scalar and bubbles in a turbulent boundary layer.

the wall-normal concentration profiles scaled with λ. Figure 20 plots y/λ versus concentration for the DNS and passive scalar results at different streamwise locations in the intermediate zone. The bubble data that are nearest injection do not collapse onto the same curve, but the results that are further downstream collapse to a curve very similar to that of the passive scalar results. However, very near the wall the bubble concentration approaches zero while the passive scalar concentration reaches a maximum value. In the transition zone, the scaling of wall-normal distance changes from λ, the scaling of the intermediate zone, to δ_{99}, the scaling of the final zone. Figure 21(a) plots y/λ versus concentration for the DNS and passive scalar results at different streamwise locations in the transition zone. The bubble data collapse on a curve very similar to that of the passive scalar results, except very near the wall where the bubble concentration approaches zero. When scaled with δ_{99} [Fig. 21(b)], the bubble data begin to collapse, with the most downstream results most closely resembling the behavior of a passive scalar in the final zone.

IV. CONCLUSIONS

Experiments[4,7,8] have shown that in high Reynolds number, spatially evolving turbulent boundary layers, microbubbles tend to migrate away from the wall as they travel downstream of injection and the skin-friction drag coefficient approaches that of a single-phase turbulent boundary layer. Simulations of bubbles injected into a spatially evolving turbulent boundary layer were performed using a one-way coupled Euler–Lagrangian approach, with parameters of the simulation chosen to reproduce the low gas-flux, high flow-speed case in the experiments of Sanders *et al.*[7] Although the Reynolds number of the simulations was lower than the experiment, the bubbles moved away from the wall, which is consistent with the experimental results. In simulations where bubbles were injected into a laminar boundary layer, the bubbles traveled toward the wall, the opposite of what is found in the turbulent simulations and in the experiments of Sanders *et al.*[7]

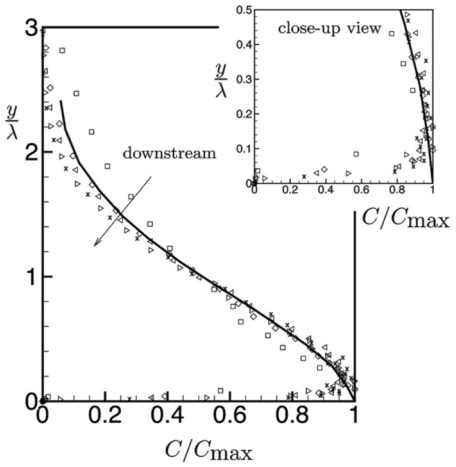

FIG. 20. Concentration profiles for a passive scalar and bubbles in the intermediate zone of a turbulent boundary layer, with the inset figure plotting a near-wall close-up view. $x/L_{ref}=(7.5,9.4,11.2,13.1,15.0)=(\square, \diamond, \triangleleft, \triangleright, x)$. —, Poreh and Cermak (Ref. 28) intermediate zone.

Budgets of the ensemble-averaged bubble acceleration showed that the largest accelerations in the wall-normal direction were due to the drag and fluid acceleration terms. The drag acceleration and buoyancy acted to push the bubbles toward the wall. Downstream of injection, the lift acceleration pushed the bubbles toward the wall. The fluid acceleration was larger than other accelerations and pushed the bubbles away from the wall. The wall-normal bubble acceleration budget shows that the tendency for bubbles to move away from the wall is due to the fluid acceleration pushing the bubbles away from the wall. Investigation into the mean and fluctuating contributions into the bubble accelerations lead to a reduction of the full equations to approximate equations for the movement of bubbles away from the wall.

In this bubbly turbulent boundary-layer flow, the behavior between bubbles and passive scalars is qualitatively similar, except very near the wall where the bubble concentration approaches zero. Bubble concentration profiles collapsed when normalizing results with length scales (such as boundary-layer thickness δ_{99} and concentration height λ) that also collapsed passive scalar profiles in Poreh and Cermak.[28] For passive scalars in flows with moderate to large Reynolds numbers and large Schmidt numbers, the transport by the local fluid drives the diffusion. For bubble diffusion, the fluid acceleration is the dominant mechanism. The importance of the fluid transport in the diffusion of bubble and passive scalars explains the similar behavior of bubbles and a passive scalar in a turbulent boundary layer.

In the experiment of Sanders *et al.*,[7] the bubble sizes are not monodisperse but have a distribution of sizes. For simplicity, a uniform bubble size equal to the mean was used in the simulation. To account for differences in bubble size, simulations with three different bubble sizes were performed. This range of bubble sizes accounts for 86% of the bubble sizes in the experiment of Sanders *et al.*[7] This simulation showed that the ensemble-averaged path of all bubble sizes moved away from the wall with increasing downstream distance. The larger bubbles ($R/\delta_{99,inj}=0.0092$) have an

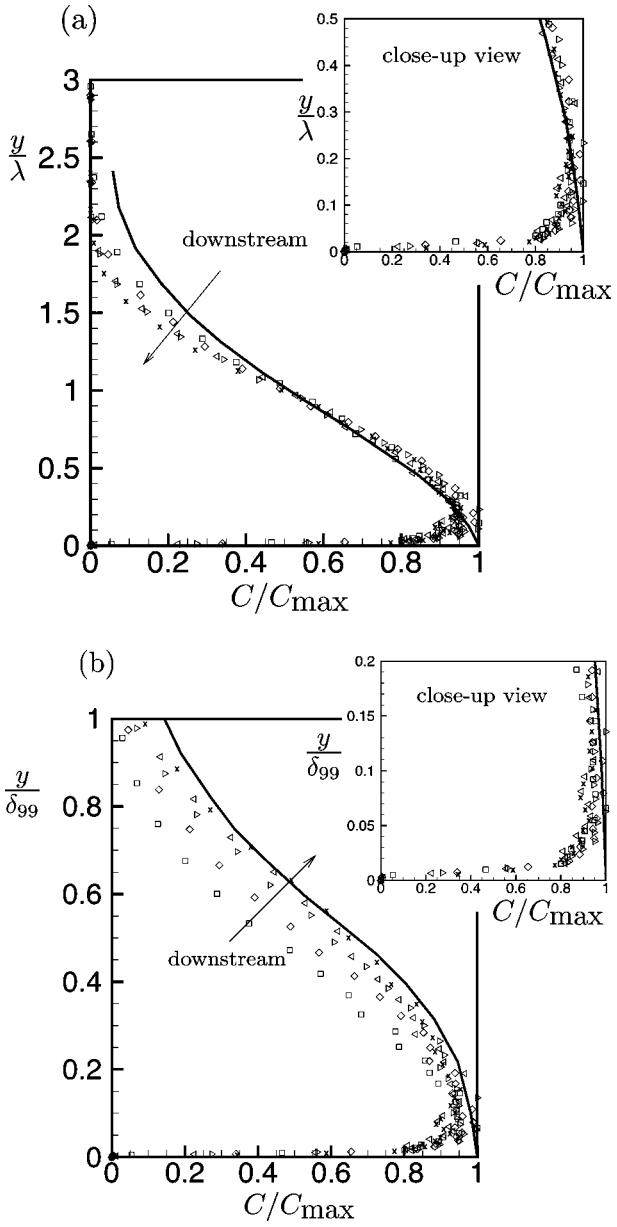

FIG. 21. Concentration profiles for a passive scalar and bubbles in the transition zone of a turbulent boundary layer. (a) shows the results for scaling using λ, with the inset figure plotting a near-wall close-up view. $x/L_{ref}=(17.5,22.5,27.5,32.5,37.5)=(\square, \diamond, \triangleright, \triangleleft, x)$. —, Poreh and Cermak (Ref. 28) intermediate zone. (b) shows scaling with δ_{99}, with the inset figure plotting a near-wall close-up view. $x/L_{ref}=(17.5,22.5,27.5,32.5,37.5)=(\square, \diamond, \triangleright, \triangleleft, x)$. —, Poreh and Cermak (Ref. 28) final zone.

ensemble-averaged path that is farther away from the wall than smaller bubbles ($R/\delta_{99,inj}=0.0037,0.0064$).

As local void fraction increases, two-way coupling effects are likely to become important. The two-way coupling effect of the bubbles on the turbulent flow has been demonstrated in Jacob *et al.*[6] In this experiment, the shear stress at the wall and the Reynolds stress near the wall have been reduced downstream of injection as compared to the single-phase experiment due to the presence of the bubbles. Although the near-wall turbulence has been modified, the profiles of the turbulent statistics of the fluid flow qualitatively resemble single-phase turbulent profiles near the wall and

approach the values of single-phase turbulence away from the wall. Therefore, it is likely that the fluid acceleration will still be the mechanism for bubble dispersion away from the wall.

ACKNOWLEDGMENTS

This work is supported by the United States Office of Naval Research under ONR Grant No. N00014-07-1-0420 with Dr. Ki-Han Kim as technical monitor. Computing resources were provided by the Arctic Research Supercomputing Center and the Minnesota Supercomputing Institute.

[1]M. E. McCormick and R. Bhattacharyya, "Drag reduction of a submersible hull by electrolysis," Nav. Eng. J. **85**, 11 (1973).
[2]C. L. Merkle and S. Deutsch, "Microbubble drag reduction in liquid turbulent boundary layers," Appl. Mech. Rev. **45**, 103 (1992).
[3]S. Ceccio, "Friction drag reduction of external flows with bubble and gas injection," Annu. Rev. Fluid Mech. **42**, 183 (2010).
[4]N. K. Madavan, S. Deutsch, and C. L. Merkle, "Measurements of local skin friction in a microbubble-modified turbulent boundary layer," J. Fluid Mech. **156**, 237 (1985).
[5]C. Gabillet, C. Colin, and J. Fabre, "Experimental study of bubble injection in a turbulent boundary layer," Int. J. Multiphase Flow **28**, 553 (2002).
[6]B. Jacob, A. Olivieri, M. Miozzi, E. F. Campana, and R. Piva, "Drag reduction by microbubbles in a turbulent boundary layer," Phys. Fluids **22**, 115104 (2010).
[7]W. C. Sanders, E. S. Winkel, D. R. Dowling, M. Perlin, and S. L. Ceccio, "Bubble friction drag reduction in a high-Reynolds-number flat-plate turbulent boundary layer," J. Fluid Mech. **552**, 353 (2006).
[8]S. Pal, C. L. Merkle, and S. Deutsch, "Bubble characteristics and trajectories in a microbubble boundary layer," Phys. Fluids **31**, 744 (1988).
[9]J. Xu, M. R. Maxey, and G. Karniadakis, "Numerical simulation of turbulent drag reduction using micro-bubbles," J. Fluid Mech. **468**, 271 (2002).
[10]A. Ferrante and S. Elghobashi, "On the physical mechanisms of drag reduction in a spatially developing turbulent boundary layer laden with microbubbles," J. Fluid Mech. **503**, 345 (2004).
[11]A. Ferrante and S. Elghobashi, "Reynolds number effect on drag reduction in a microbubble-laden spatially developing turbulent boundary layer," J. Fluid Mech. **543**, 93 (2005).
[12]J. Lu, A. Fernández, and G. Tryggvason, "The effect of bubbles on the wall drag in a turbulent channel flow," Phys. Fluids **17**, 095102 (2005).
[13]W. C. Sanders, "Bubble drag reduction in a flat plate boundary layer at high Reynolds numbers and large scales," Ph.D. thesis, University of Michigan, 2004.
[14]K. Mahesh, G. Constantinescu, and P. Moin, "A numerical method for large-eddy simulation in complex geometries," J. Comput. Phys. **197**, 215 (2004).
[15]V. E. Johnson, Jr. and T. Hsieh, "The influence of the trajectories of gas nuclei on cavitation inception," Sixth Naval Hydrodynamics Symposium, 1966, p. 163.
[16]N. H. Thomas, T. R. Auton, K. Sene, and J. C. R. Hunt, "Entrapment and transport of bubbles by plunging water," in *Gas Transfer at Water Surfaces*, edited by W. Brutsaert and G. H. Jirka (Reidel, Dordrecht, 1984), pp. 255–268.
[17]T. R. Auton, J. C. R. Hunt, and M. Prud'homme, "The force exerted on a body in inviscid unsteady non-uniform rotational flow," J. Fluid Mech. **197**, 241 (1988).
[18]W. L. Haberman and R. K. Morton, "An experimental investigation of the drag and shape of air bubbles rising in various liquids," David W. Taylor Model Basin Report No. 802, 1953.
[19]T. R. Auton, "The lift force on a spherical body in a rotational flow," J. Fluid Mech. **183**, 199 (1987).
[20]G. K. Batchelor, *An Introduction to Fluid Dynamics* (Cambridge University Press, Cambridge, 1967), pp. 404–409.
[21]G. Sridhar and J. Katz, "Drag and lift forces on microscopic bubbles entrained by a vortex," Phys. Fluids **7**, 389 (1995).
[22]D. Legendre and J. Magnaudet, "The lift force on a spherical bubble in a viscous linear shear flow," J. Fluid Mech. **368**, 81 (1998).
[23]T. S. Lund, X. Wu, and K. D. Squires, "Generation of turbulent inflow data for spatially-developing boundary layer simulations," J. Comput. Phys. **140**, 233 (1998).
[24]M. P. Simens, J. Jiménez, S. Hoyas, and Y. Mizuno, "A high-resolution code for turbulent boundary layers," J. Comput. Phys. **228**, 4218 (2009).
[25]M. R. Maxey, E. J. Chang, and L.-P. Wang, "Interactions of particles and microbubbles with turbulence," Exp. Therm. Fluid Sci. **12**, 417 (1996).
[26]M. R. Head and P. Bandyopadhyay, "New aspects of turbulent boundary-layer structure," J. Fluid Mech. **107**, 297 (1981).
[27]H. Schlichting, *Boundary-Layer Theory*, 7th ed. (McGraw-Hill, New York, 1979), pp. 135–144.
[28]M. Poreh and J. E. Cermak, "Study of diffusion from a line source in a turbulent boundary layer," Int. J. Heat Mass Transfer **7**, 1083 (1964).
[29]K. Wieghardt, "Über ausbreitungsvorgänge in turbulenten reibungsschichten," Z. Angew. Math. Mech. **28**, 346 (1948).